Materials Research Bulletin 143 (2021) 111442

Contents lists available at ScienceDirect

Materials Research Bulletin

journal homepage: www.elsevier.com/locate/matresbu

Unraveling the relationship between bulk structure and exposed surfaces and its effect on the electronic structure and photoluminescent properties of $Ba_{0.5}Sr_{0.5}TiO_3$: A joint experimental and theoretical approach

Weber Duarte Mesquita [a], Marisa Carvalho de Oliveira [b,*], Marcelo Assis [b,c], Renan Augusto Pontes Ribeiro [d], Ariadne Canedo Eduardo [a], Marcio Daldin Teodoro [e], Gilmar Eugenio Marques [e], Mário Godinho Júnior [a,f], Elson Longo [b], Maria Fernanda do Carmo Gurgel [a,f]

[a] Institute of Physics, PPGCET, Federal University of Catalão, Av. Dr. Lamartine Pinto de Avelar, Catalão, GO 75704-020, Brazil
[b] Functional Materials Development Center, Federal University of São Carlos, São Carlos, SP 13565-905, Brazil
[c] Department of Physical and Analytical Chemistry, University Jaume I, Castelló 12071, Spain
[d] Department of Chemistry, State University of Minas Gerais, Av. Paraná, Divinópolis, MG 35501-170, Brazil
[e] Department of Physics, Federal University of São Carlos, São Carlos, SP 13565-905, Brazil
[f] Institute of Chemistry, Federal University of Catalão, Av. Dr. Lamartine Pinto de Avelar, Catalão, GO 75704-020, Brazil

ARTICLE INFO

Keywords:
$Ba_{0.5}Sr_{0.5}TiO_3$ perovskite
(001) Surface
DFT calculations
Band-gap
Photoluminescence

ABSTRACT

In this paper, we conducted a combined experimental and theoretical investigation of bulk and (001) surface properties of a $Ba_{0.5}Sr_{0.5}TiO_3$ (BST) material synthesized by the polymeric precursor method. Characterization techniques, such as X-ray diffraction (XRD), Raman spectroscopy, ultraviolet-visible diffuse reflectance spectroscopy, field-emission scanning electron microscopy (FE-SEM) and photoluminescence (PL), were employed to disclose the structural, electronic, and optical properties of BST. Structural analysis confirmed the BST tetragonal symmetry, showing the relevant fingerprints of structural distortions, while the crystallographic morphologies were observed in the FE-SEM images. The theoretical results evidenced the structural disorder along the tetragonal BST phase, corroborating the central role of the bonding environment in the electronic and PL properties of the material. Moreover, the (001) surface results indicated that $\mathbf{E_{surf}}$ values depend on the chemical environment of exposed surfaces following the bonding character along with A-O and Ti-O paths, which also affects the electronic structure of surface-oriented BST.

1. Introduction

A great variety of metallic ions can occupy the A and B sites in the technologically crucial ABO_3 perovskite structure. Such versatility of this class of materials makes them a perfect choice for a large number of catalytic applications, including electronic devices, such as energy storage capacitors, infrared detectors and chemical sensors, as well as microwave tunable applications, such as phase shifters, tunable filters and tunable resonators [1–6]. For many of those ABO_3 perovskite applications, surface quality and structure play essential roles. For example, recent studies have shown that the catalytic properties of ABO_3 perovskite oxides are related mainly to oxygen vacancies, which alter their electronic and crystalline structures and surface chemistry [7–12]. Forefront (001) surfaces and interface phenomena, which occur in the ABO_3 perovskite oxides and their nanostructures, are hot topics in modern solid-state physics due to their desirable atomic and electronic processes.

Following the development of new and emerging technologies, the atomic and electronic properties, as well as the structure of ABO_3 perovskite (001) surfaces, have been intensively and experimentally explored during the last years through the combination of different techniques [13–19]. Moreover, in the past few years, the scientific interest regarding quantum-mechanical simulations for perovskite surfaces has increased due to the precise atomic-level representation of the major mechanism involved in the surface stabilization and the control of reactivity based on surface-dependent physical and chemical properties that govern many kinds of technological applications [11,12,20–26].

The general formula of perovskite compounds is ABX_3, where A is

* Corresponding author.
E-mail address: marisa-coliveira@hotmail.com (M.C. de Oliveira).

https://doi.org/10.1016/j.materresbull.2021.111442
Received 22 January 2021; Received in revised form 25 May 2021; Accepted 13 June 2021
Available online 16 June 2021

mono or divalent cation, B is a tetra or pentavalent cation, and X is the halide anion. The ideal structure of oxides presents cubic geometry with a 221 (*Pm-3m*) space group. More specifically, the A cation is located in the unit cell corners coordinated with twelve O anions forming [AO_{12}] clusters, while the smaller B cation coordinates with six O anions to generate [BO_6] units in the center position of the unit cell [27–29]. The A- and B-site substitution is a widespread strategy to induce a structural distortion resulting from the partial replacement of A and/or B cations by dopants of different sizes and valences, causing alterations in the perovskite traditional formula ABO_3 to $A_{1-x}A'_xB_{1-y}B'_yO_3$ or $AB'_{1-x}B''_xO_3$. In particular, such changes, along with the different atomic sites, often cause significant alterations in the structural, chemical, and physical properties of the materials [30–32]. For example, in Barium Strontium Titanate ($Ba_{1-x}Sr_xTiO_3$, BST), the lower strontium concentration induces the stabilization of the ferroelectric properties of a tetragonal geometry, whereas the composition corresponding to the higher strontium content is cubic and paraelectric [33].

Conventionally, BST solid solution can be prepared by the solid-state reaction from $BaTiO_3$ and $SrTiO_3$ materials [34]. At room temperature, $SrTiO_3$ has a cubic perovskite structure with a Curie point at low temperature (218.15 K) [35]. The Curie point of $BaTiO_3$ was described as 393.15 K. Depending on the temperature range, $BaTiO_3$ undergoes a successive phase transition involving cubic, tetragonal, orthorhombic, and rhombohedral phases. Above the Curie point, the original cubic symmetry is stable [36]. The first-principle study of the temperature effects proposed by Oliveira et al. confirms the phase transition in $BaTiO_3$, based on the combination of structural distortion in [TiO_6] clusters, vibrational characteristics, and electronic structure [37]. Following such observation, BST experimental results have indicated a phase transition similar to $BaTiO_3$ depending on the Sr content [38]. Despite the scientific efforts to investigate the BST structure and properties, a detailed analysis of the mechanisms associated with its intriguing physical and chemical properties remains debatable, motivating the search for a systematic explanation of the global effects that control the bulk and surface properties of perovskite materials.

For this purpose, in this work, we demonstrate the synthesis of BST perovskite materials by the polymeric precursor method (PPM). The samples were annealed at different temperatures (400-700 °C) for 2 h to investigate the order-disorder associated with the heat treatments. Various analyses, such as Raman spectroscopy, X-ray diffraction (XRD), UV-Vis spectrometry, field-emission scanning electron microscopy (FE-SEM), and photoluminescence (PL) were carried out to monitor the structural disorder effects. Moreover, first-principles quantum-mechanical calculations were performed to determine the BST bulk and surface models and their structural and electronic properties. The theoretical study investigates the electronic structure of BST models and gives an interpretation in terms of band structure, the density of states (DOS) with atomic orbitals, hybridization, and charge density distribution analysis.

Additionally, first-principle calculations of the four possible (001) surface terminations of $Ba_{0.5}Sr_{0.5}TiO_3$ (BST) perovskites are presented. This complementary approach renders a plausible quantitative description of BST electronic behavior and an interesting correlation between the theoretical and experimental results. This research involves five critical steps: (1) synthesis of powders, (2) theoretical modeling, (3) structural characterization, (4) electronic and optical properties, and (5) the main conclusion of our work.

2. Methodology

2.1. Experimental procedure and characterization

$Ba_{0.5}Sr_{0.5}TiO_3$ (BST) powders were prepared by the polymeric precursor method (PPM), which is based on the chelation of metal cations and citric acid ($C_6H_8O_7$, 99.5%, Synth) in a solution of water and ethylene glycol ($C_2H_6O_2$, 99.5%, Synth). Barium carbonate ($BaCO_3$, 99.9%, Aldrich), strontium carbonate ($SrCO_3$, 99.9%, Aldrich), and titanium isopropoxide ($C_{12}H_{28}O_4Ti$, 97%, Aldrich) were used as raw materials.

The dissolution of titanium isopropoxide formed titanium citrate in an aqueous solution of citric acid ($C_6H_8O_7$) between 70 °C and 90 °C. Then, a stoichiometric amount of $BaCO_3$ and $SrCO_3$ was added. To prevent CO_3 precipitation, cationic precursors were slowly added to the titanium citrate under constant stirring at 80 °C. The complete dissolution of the cationic precursors resulted in a transparent solution.

Ethylene glycol was added after homogenization of the solution containing Ba^{2+}, Sr^{2+}, and Ti^{4+} cations to promote polymerization of the mixed citrates by polyesterification. Upon continuous heating at 80 °C, the solution became more viscous, forming a polymeric resin with no visible phase separation. The molar ratio between Ba, Sr, and Ti was 1:1, and the citric acid/ethylene glycol ratio was set to 60/40 mass.

The resin was placed in a conventional furnace for heat treatment at 350 °C for 4 h for organic matter decomposition. These polymeric precursors were deagglomerated, and the heat treatment was carried out at various temperatures (from 400 to 700 °C) for 2 h under ambient atmosphere.

The BST powders were characterized by X-ray diffraction using a Rigaku Dmax 2500PC diffractometer with Cu Kα radiation (λ =1.5406 Å). The obtained results were compared with the International Centre for Diffraction Data (ICDD). Raman data were recorded using a Bruker RFS/100/S spectrometer with an Nd:YAG laser producing a 1064.0 nm excitation light. The UV-Vis absorption spectra of the optical absorbance for disordered BST powders were taken using Cary 5G equipment. Photoluminescence measurements were performed at room temperature using a 355 nm laser (Cobolt/Zouk) as an excitation source focused on a 200 μm spot at a constant power of 5 mW. The luminescent signal was dispersed by a 19.3 cm spectrometer (Andor/Kymera) and detected by a silicon charge-coupled device (Andor/IdusBU2).

The temperature-dependent crystallite size of BST powders was estimated according to the XRD data using the Scherrer equation, a widely used tool to obtain crystallite size represented by the following formula:

$$\boldsymbol{D = \frac{K\lambda}{\beta\, cos\theta}} \tag{1}$$

where D is the crystallite size, K is a shape constant (0.9), θ is the Bragg angle, λ is the radiation wavelength and (0.154 nm), β is the full width at half-maximum (FWHM) of the diffraction peak [39]. In the Scherrer equation, the β parameters need to be corrected to eliminate the so-called instrumental effects [40]. The best method to make this correction uses a standard sample with a small microstrain and great particle size so that the widths of diffraction peaks observed are only due to instrumental effects [41]. The Gaussian correction was applied by comparing the FWHM of X-ray reflection between the sample and the single-crystalline Si standard to obtain the true crystal broadening: The most refined expression for this instrumental effect correction is:

$$\boldsymbol{\beta = \sqrt{\beta^2_{exp} - \beta^2_{standart}}} \tag{2}$$

where β is the true half-maximum width, β^2_{exp} and $\beta^2_{standart}$ are the half-maximum widths of the sample and the single-crystalline Si standard, respectively.

Another classical method to obtain quantitative information on particle size and microstrain considering the enlargement of diffraction peaks is through the Williamson-Hall plot (WH plot) [42].

The WH plot allows us to extract the microstrain through the angular coefficient and mean particle size using the linear coefficient (slope of the curve and the intersection of the curve with the ordinate axis, respectively), and the following equation represents their homogeneity from the angular width of peak diffraction:

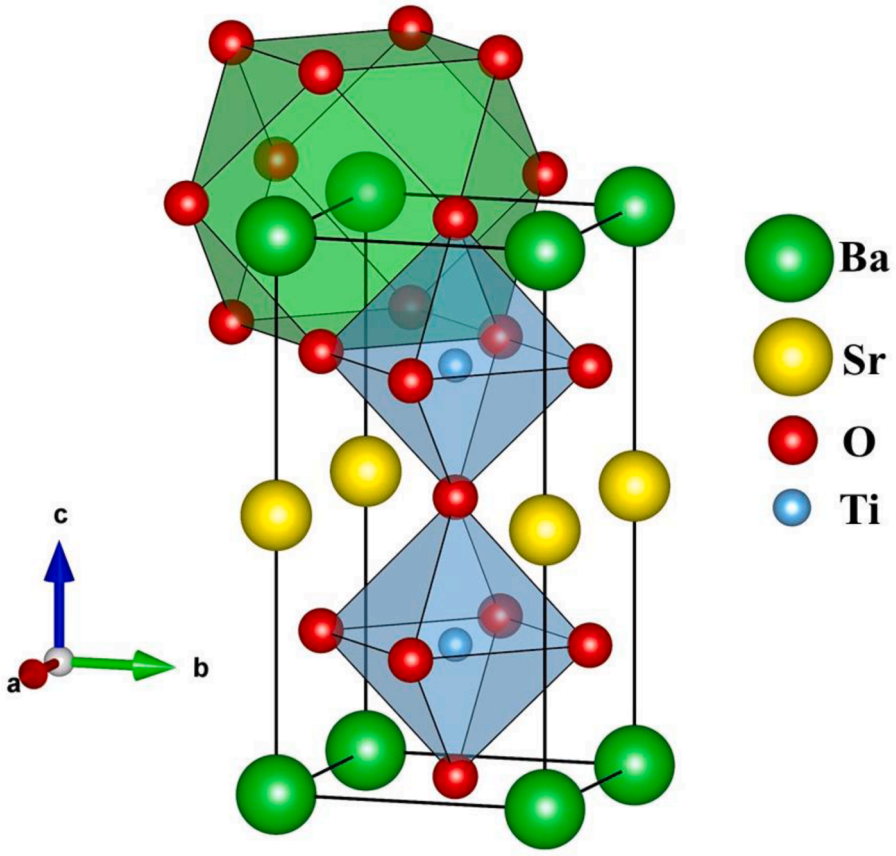

Fig. 1. 1 × 1 × 2 supercell representation of the tetragonal BST structure.

$$\frac{\beta cos\theta}{\lambda} = \frac{K}{D} + \frac{4\varepsilon}{\lambda} sen\theta \quad (3)$$

where β is the half-width of diffraction peak (FWHM), λ is the wavelength of x-ray, and K is a constant (value 1), which determines the point in the network reciprocal, D is the average size of crystalline, ε is the microstrain [42].

The morphologies and sizes of the samples were observed using a field-emission scanning electron microscope (FE-SEM) operated at 5 kV (Supra 35-VP, Carl Zeiss).

2.2. Computational details and model systems

The calculations were performed using CRYSTAL14 [43] package within the framework of the density functional theory (DFT) [44]. A gradient-corrected correlation function developed by Lee, Yang, and Parr, combined with the Becke3 exchange-correlation functional (B3LYP) [45], was used to calculate the structural parameters and perform the analysis of the electronic structure, following a series of theoretical studies for a wide variety of perovskite compounds [46–48]. According to the CRYSTAL basis set library, all-electron basis sets described the atomic centers: 9763-311_d631_G for Ba, 86-411_d31_G for Ti, 6-31G* for O, and 976-41(d51)G for Sr [49]. Vesta program was used to model the BST structure [50].

The electronic integration was performed using a 4 × 4 × 4 Monkhorst-Pack [51] k-mesh containing 75 k-points for all models. The accuracy of the Coulomb and exchange integral calculations were controlled by five thresholds set to 8, 8, 8, 8, and 16. The converge criterion for mono- and bi-electronic integrals were set to 10^{-8} Ha, while the root-mean-square (RMS) gradient, RMS displacement, maximum gradient, and maximum displacement were set to 8×10^{-5}, 1.9×10^{-4}, 1.3×10^{-4} and 3.8×10^{-4} a.u., respectively. Lattice parameters and atomic positions were fully relaxed for the 1 × 1 × 2 supercell model.

The BST material simulation was developed from unit cell expansion in the z-axis (001), obtaining a 1 × 1 × 2 supercell based on a tetragonal structure (*P4mm* - 99) composed of one Ba atom, one Sr atom, two Ti atoms, and six O atoms (Fig. 1). The Ti atoms are coordinated to six O atoms, producing an octahedral $[TiO_6]$-$[TiO_6]$ cluster, while the Ba and Sr atoms are coordinated to twelve O atoms, resulting in $[BaO_{12}]$ and $[SrO_{12}]$ clusters. Initial lattice parameters were obtained from experimental XRD using REDE93 software [52], and atomic positions were taken from the literature [53]. The theoretical optimization lattice parameters were obtained from CRYSTAL14 [43], yielding values of a = 3.930 Å and c = 3.983 Å, and angles α = β = γ = 90°. This model was used to study the structural, electronic, and optical properties of BST. The theoretical results are discussed through the density of states (DOS) orbital projections, band structure analysis, and charge density distribution following the Mulliken approach. The DOS and band structures were particularly evaluated from the last eleven energy bands in the valence band (VB) and the first eleven energy bands in the conduction band (CB), featuring the band-gap region.

Besides, vibrational analysis for ground state in the equilibrium configurations of the BST models was performed to ensure none imaginary frequencies corresponding to the saddle points on the potential energy surface. It is well known that the DFT calculation based on the B3LYP method tends to overestimate the values of the vibrational frequencies; therefore, a scaling factor of 0.94 is used [54].

The surface energy values, E_{surf}, for the (001) cleavage plane were calculated to correlate the electronic and energetic properties of BST. In this context, the BST (001) surfaces were modeled considering crystals as a set of crystalline planes perpendicular to the given surface and cutting out the 2D slab of a finite thickness, causing it to be periodic in the x–y plane. The slabs are symmetric and non-stoichiometric with respect to the unit cell. These two AO (A=Ba and Sr) and TiO_2

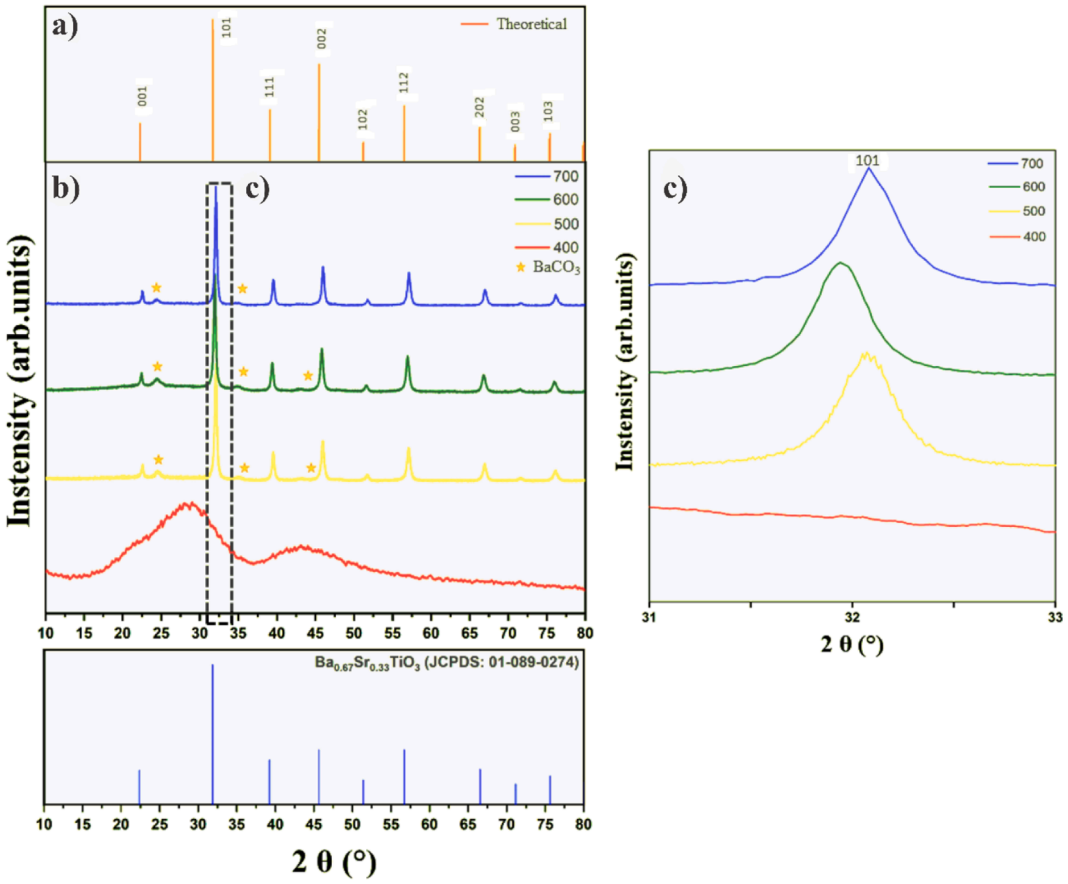

Fig. 2. XRD patterns of the BST powders: (a) theoretical, (b) experimental calcined at 400, 500, 600 and 700°C and (c) peak magnification in the region from 31° to 33°.

terminations are the only possible flat and dense (001) surface terminations of the perovskite structure.

In the present study, E_{surf} was assumed to correspond to the surface cleavage (E_{cleav}). Therefore, we firstly introduce the concept of unrelaxed E_{cleav} as the required energy to cut the bulk along the (001) plane. Our performed B3LYP ab-initio calculations started with the cleavage energy for unrelaxed AO- (A=Ba and Sr) and TiO_2-terminated (001) surfaces. Since surfaces with both terminations simultaneously arise under the (001) cleavage of the crystal, we adopted the convention that the cleavage energy is equally distributed between the created surfaces. In our calculations, the 18-layer AO-terminated (001) slab with 22 atoms and the 14-layer model for the TiO_2-terminated slab with 18 atoms represent together 8 bulk unit cells (80 atoms – $Ba_{0.5}Sr_{0.5}TiO_3$), so that:

$$E_{cleav}^{unrlx} = \frac{E_{slab}^{BaO} + E_{slab}^{TiO2-Ba} + E_{slab}^{SrO} + E_{slab}^{TiO2-Sr} - 8E_{bulk}}{8A} \quad (4)$$

where E_{slab}^{i} correspond to the unrelaxed energies of the AO- or TiO_2-terminated (001) slabs, respectively, E_{bulk} is the energy per bulk unit cell, and A represents the surface area.

Next, we calculated the relaxation energies for each AO or TiO_2 termination, according to Eq. (5)):

$$E_{relax}^{T} = \frac{E_{slab}^{T}(rlx) - E_{slab}^{T}(unrlx)}{2A} \quad (5)$$

Here, $E^{t}{}_{relax}$ is the slab energy after relaxation (T = AO or TiO_2). The surface energy is then defined as the sum of the cleavage and relaxation energies.

$$E_{surf}^{T} = E_{cleav}^{unrlx} + E_{relax}^{T}$$
$$T = BaO, Sro, TiO_2 - Ba, TiO_2 9 - Sr \quad (6)$$

This methodology has been successful for the study of the E_{surf} of various materials, including perovskites and several other oxides [11,24,55].

In order to analyze the relationship between E_{surf} and the geometric characteristics of the exposed surfaces, the dangling bond density (D_b) was calculated from the number of broken bonds created per unit cell (N_b) on a particular surface of area **A** [56], according to the expression:

$$D_b \frac{N_b}{A} \quad (7)$$

3. Results and discussion

3.1. X-ray diffraction

Fig. 2a–c show the simulated and experimental XRD patterns of the BST powders calcined at 400, 500, 600, and 700 °C for 2h. Herein, the simulated XRD patterns were obtained using VESTA software. The XRD simulation is in good agreement with the ICDD crystallographic card number 01-089-0274 [57] and the experimental data obtained at 700 °C. The powders obtained at 400 °C displayed a typical amorphous pattern due to the formation of a disordered material, presenting a broad band centered at 2θ = 28.65°. Samples heated at 500, 600, and 700 °C for 2h exhibited diffraction peaks related to two different phases: BST and $BaCO_3$. The formation of $BaCO_3$ (orthorhombic structure) – ICDD 01-070-6454 [58] – as an intermediate phase results from the reductive atmosphere arising from organic precursors during heat treatment.

The XRD patterns of the BST models showed polycrystalline phases

Table 1
Theoretical, experimental (REDE93) and literature lattice parameters.

BST samples				
Lattice Parameters	500 °C	600 °C	700 °C	Theoretical
a = b (Å)	3.951	3.958	3.980	3.930
c (Å)	3.950	3.952	3.986	3.983
Percentual error (%)				
a = b (Å)	0.53	0.712	1.272	–
c (Å)	0.82	0.77	0.075	–
Literature				
a = b (Å)	3.969	4.017	3.979	3.995
c (Å)	3.958	3.9804	3.996	3.988
Reference	[67]	[68]	[69]	[70]

of tetragonal perovskite material, as confirmed by the reflection angle planes as illustrated in Fig. 2a and b. The lattice parameters of the tetragonal unit cells were determined from the 0 0 1; 1 0 1; 1 1 1; 0 0 2; 1 0 2; 1 1 2; 2 0 2; 0 0 3 and 1 0 3 planes, utilizing REDE93 software program, developed at the Chemistry Institute of Unesp in Araraquara, SP, Brazil by Paiva-Santos et al. [52] This program, which is based on the square method, refines the position of diffraction peaks. Based on XRD patterns, the values of lattice parameters are depicted in Table 1. Several studies reported using REDE93 software to determine lattice parameters for different materials [59–66].

It can be observed in Table 1, the crystal structure and the lattice parameters of theoretical results exhibit a small mean percentage error in comparison with the experimental and literature results, evidencing that our calculations are in good agreement with experimental data. Therefore, the BST samples should be ferroelectric at room temperature and with a slightly distorted tetragonal structure [71].

In addition, Fig. 2c shows the peak magnification in the region from 31° to 33° related to the effect of replacement of Ba^{2+} by Sr^{2+} in the BT for powders calcined at different temperatures. In all powders, the strongest peak at around 2θ = 31.8-32° corresponds to the 101 crystalline plane, where a slight displacement can be observed as the temperature increases. The effect of structural order-disorder with increasing temperature was verified by narrowing the peak corresponding to the 101 plane. Moreover, the change in the lattice is due to the distinct electronic density concerning Ba^{2+} ions and the introduction of structural defects with the formation of $[SrO_{12}]$ clusters. According to the XRD patterns for BST, when a few Ba^{2+} ions are replaced by Sr^{2+} ions, the lattice structure slightly changes because of the ionic radius of Sr^{2+} (1.44 Å), which is slightly smaller than that of Ba^{2+} (1.61 Å) [33,70,72].

The results of Williamson-Hall analysis for BST samples are shown in Fig. 3. A moderate strain anisotropy is obtained. The plots indicate that the 500 °C, 600 °C, and 700 °C BST samples exhibit a positive slope indicating the possibility of tensile strain in the samples. The calculated strains in these BST samples are estimated to be 9.74×10^{-4}, 1.11×10^{-3}, and 4.39×10^{-3}, respectively. The calculated crystallite size values for 500 °C, 600 °C, and 700 °C are 25.91, 26.01, and 34.06 nm, respectively. These values are described in Table S1.

There is a slight variation in the effective crystallite size for samples obtained by Scherrer obtained by the WH method (Table S1). The difference may be due to internal strain not considered in the Scherrer model [73].

In 700 °C BST samples, the crystallite size value calculated by the WH method is comparatively larger than those calculated by the Scherrer formula. This enlargement of values may be attributed to the tensile strain taken into consideration in the Williamson-Hall analysis.

Additionally, all BST samples in Fig. 3 show expansive unit cells due to positive values with temperature increment. Table S1 summarizes the crystallite sizes and strain values of the BST powders obtained using the Scherrer equation and WH method. The values showing nanometric sizes range from 28.34 nm to 30.22 nm and 25.91 nm to 34.06 nm for Scherrer and Williamson-Hall methods, respectively. As a result, the Scherrer equation provides values that are in good agreement with the WH graph. The stepwise heat treatment of these samples significantly increases the intensity of Bragg reflections and decreases their widths, evidencing an increase in the average size of ceramic crystallites since

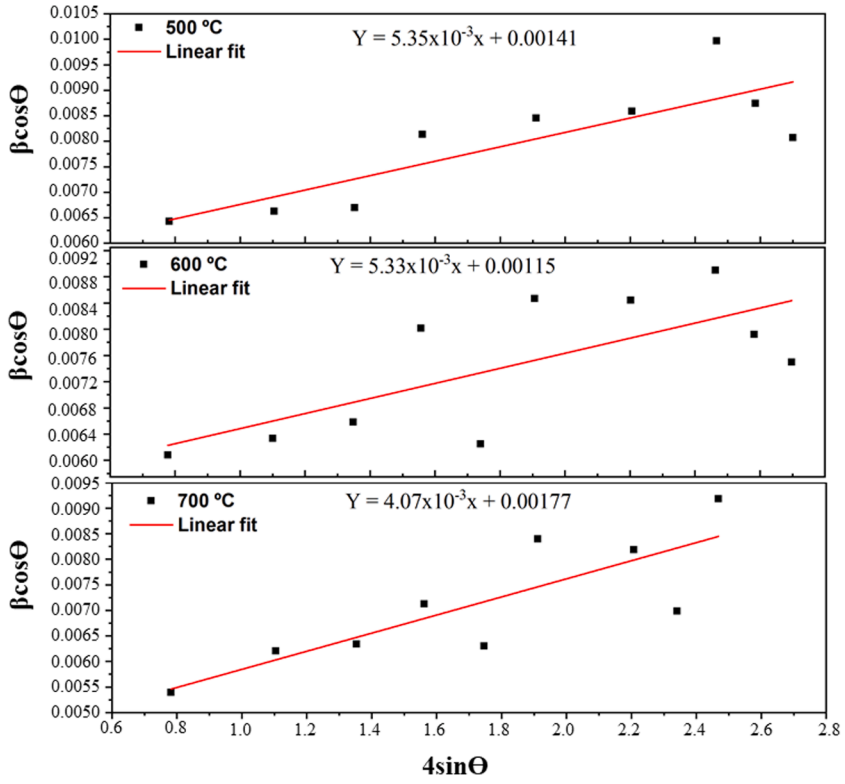

Fig. 3. Williamson-Hall plots of BST calcined at 500, 600 and 700 °C.

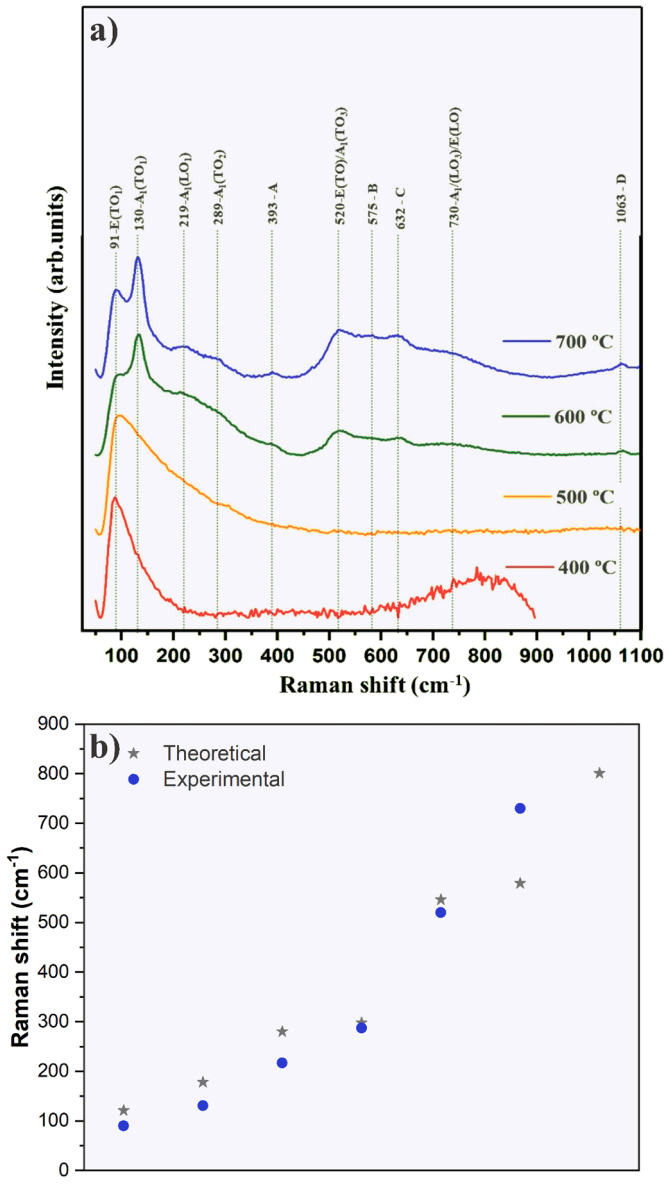

Fig. 4. Raman spectrum of the BST material: (a) experimental heat-treated at 400, 500, 600 and 700 °C for 2 h and (b) comparative theoretical-experimental Raman-active modes.

the high energy supplied from the high synthesis temperatures improves nucleation and crystallite growth. Similar results were obtained by Dutra et al. [74].

3.2. Raman analysis

Raman spectroscopy is an excellent complementary characterization tool to identify phase evolution through the Sr substitution function in the $BaTiO_3$ lattice. $BaTiO_3$ has five atoms and fifteen degrees of freedom per unit cell. In the cubic phase, the O_h^1 symmetry has an irreducible representation of 12 optical modes ($3F_{1u} + 1F_{2u}$). The F_{1u} modes are infrared-active, while the F_{2u} mode is silent since neither is infrared- nor Raman-active. At room temperature, $BaTiO_3$ is tetragonal with C_{4v} symmetry. Based on the crystallography, the Raman-active modes for tetragonal $BaTiO_3$ (P*4mm*) are $4E(TO+LO) + 3A_1(TO+LO) + B_1(TO+LO)$. All of the A_1 and E modes are Raman- and infrared-active, whereas the B_1 mode is only Raman-active. The transverse and longitudinal optical components (TO and LO) occur with the presence of long-range electrostatic forces that further split each of the A_1 and E modes [75,76].

Fig. 4a shows the experimental Raman spectra of tetragonal BST powders in a frequency range of 25-1100 cm^{-1} at 400, 500, 600, and 700°C. We can observe six active modes: $E(TO_1)$ at ~91 cm^{-1}, $A_1(TO_1)$ at ~130 cm^{-1}, $A_1(LO_1)$ at ~219 cm^{-1}, $A_1(TO_2)$ at ~289 cm^{-1}, $E(TO)/A_1(TO_3)$ at ~520 cm^{-1} and $A_1(LO_3)/E(LO)$ at ~730 cm^{-1}. At a calcination temperature of 400 and 500 °C, it is possible to note structural disorder for the obtained powders. On the other hand, the powders annealed at 600 and 700 °C result in the tetragonal perovskite phase. Thus, the Raman-active vibrational modes confirm the short-range order for the BST tetragonal perovskite phase. These results are in agreement with the XRD patterns for the BST samples.

The experimental and calculated Raman-active modes are shown in Fig. 4b, where a strong interaction between the ions arising from the stretching and bending vibrations of the shorter metal-oxygen bonds within the anionic groups can be observed. The calculated Raman spectra of the BST at the B3LYP level of theory in the frequency range of 100-900 cm^{-1} are illustrated in Fig. S1. In the Raman spectrum of the tetragonal BST crystal structure, we can observe seven active vibration modes at 121, 178, 280, 298, 546, 579, and 801 cm^{-1}.

Table 2 represents the frequencies of the BST Raman-active modes, which are in agreement with the literature.

Furthermore, the Raman spectra of the BST samples are very similar to the bulk BT [77], except for the non-identification of B_1 and E (TO+LO) and $A_1(LO_2)$ and E(LO) active components, typical of the $BaTiO_3$ structure. Additionally, the two asymmetric broad $A_1(TO)$ modes at 289 and 520 cm^{-1} are associated with structural defects. On the other hand, the high intensity of the $A_1(TO_1)$ mode and low intensity of the $A_1(LO_3)$ and E(LO) components in BST evidences that the BT doping with Sr causes an increase in crystal symmetry. The $E(TO_1)$ and $A_1(TO_2)$ components at 91 and 289 cm^{-1}, respectively, are associated with the tetragonal-cubic phase transition, while the low intensity of $A_1(LO_3)$ and E(LO) is closely related to the tetragonality factor. At last, the lattice parameter distortion is associated with $A_1(LO_1)$.

In the Raman spectra in Fig. 4a, it is possible to note three additional disorder-active bands centered at ~393, ~575, and ~632 cm^{-1}, marked as A, B, and C, respectively, and another one at 1063 cm^{-1}, marked as D,

Table 2
Raman-active modes (cm^{-1}) for BST powders heat-treated at 400, 500, 600 and 700°C for 2 h.

Raman active modes	Experimental (BST 700 °C) (cm^{-1}) *This work*	BTO (cm^{-1}) [77]	BST (cm^{-1}) [78]	BST (cm^{-1}) [79]	BST (cm^{-1}) [80]	BST (cm^{-1}) [81]
$E(TO_1)$	91	-	112	-	97	-
$A_1(TO_1)$	130	155	150	176	155	181
$A_1(LO_1)$	219	189	-	-	174	-
$A_1(TO_2)$	289	260	201	221	191	227
B1 and E(TO+LO)	-	305	287	294	294	304
$A_1(LO_2)$ and E(LO)	-	470	-	-	476	-
E(TO) and $A_1(TO_3)$	520	518	517	516	535	528
$A_1(LO_3)$ and E(LO)	730	718	731	732	747	730

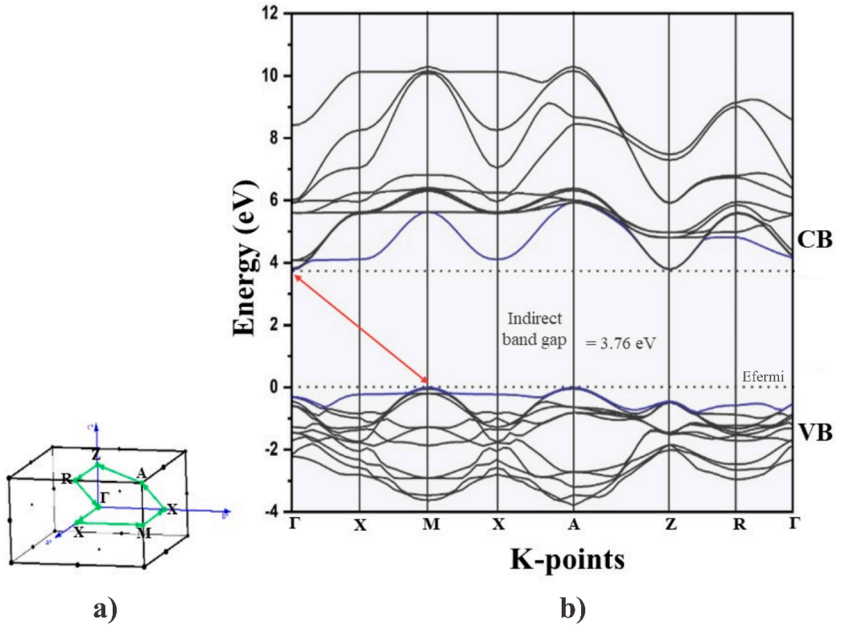

Fig. 5. **(a)** Primitive cell Brillouin zone, and **(b)** band structure profiles for the 1x1x2 supercell of the BST model.

which is related to the carbonate ions [82]. These results are confirmed by the slight displacements in the [TiO_8] clusters due to the Ba/Sr substitution with partial loss of translational symmetry of the BST powders. In particular, the same behavior was observed by Katiyar et al. [83].

3.3. Optical band-gap analysis

The optical properties of the BST samples were investigated using UV-Vis at 400, 500, 600, and 700°C for 2h. With the partial replacement of Ba^{2+} by Sr^{2+} ions, a considerable change in the crystalline environment can occur involving the electronic and structural properties of materials, as shown in Fig. S2.

The energy values presented in Fig. S2 were determined by the Wood and Tauc method [84], following the equation:

$$\mathbf{h}\nu\alpha \propto \left(\mathbf{h}\nu - \mathbf{E}_{\mathbf{gap}}^{\mathbf{opt}}\right) \quad (8)$$

where **α** is the absorbance, **h** is the Planck constant, ν is the frequency and E_{gap}^{opt} is the optical band-gap.

The results of the experiments show that the E_{gap} increases as a function of temperature from 2.14 eV to 3.06 eV, 3.11 eV, and 3.12 eV at 400, 500, 600, and 700°C, respectively. Structural order-disorder parameters can explain the band-gap energy increase of BST. For BST samples heat-treated at 400, 500, 600, and 700°C, we observed typical absorption spectra for quasi-crystalline and crystalline materials, or an ordered structure (Fig. 2), indicating that the increase of structural organization in the lattice leads to the reduction of these intermediary energy levels, and consequently to an increase in the E_{gap} value. In addition, the different E_{gap} values with increasing temperature can be related to other factors, such as the preparation method, powder shape, particle morphology, heat treatment temperature, and processing time. These factors result in different structural defects and can promote intermediate levels within the band-gap. In contrast to the ideal semiconductor absorption that should present a vertical line for this electronic transition, it can be observed that all samples have high defect density due to a remarkable inclination of the Urbach tail [85]. These defects are directly related to the distortions at the bond angles of the building block clusters.

Table 3
Calculated and experimental values of the band-gap energy of BST.

Compounds BST	Reference	Band-gap (eV)	Percentual error (%)
Theoretical	This work	3.76	–
Experimental at 700°C	This work	3.12	20.5
Literature	[86]	3.30	13.9
	[87]	3.47	8.35
	[88]	3.69	1.89

3.4. Electronic structure by DFT computational simulations

3.4.1. Band structure analysis

The primitive cell Brillouin zone and band structure obtained for the BST models are displayed in Fig. 5a and b. In the primitive cell Brillouin zone (Fig. 5a) we have chosen the Γ, X, M, X, A, Z, R and Γ points, beginning at (Γ = 0,0,0), (X = ½,0,0), (M = ½, ½,0), (X = 0, ½,0), (A = ½,½,½), (Z = 0,0, ½) and (R = ½,0, ½) as the reciprocal coordinates.

According to the band structure representation in Fig. 5b, the VB can be observed between -4 and 0 eV, while the CB values range from 3.76 to 12 eV. The calculated indirect band-gap energies were obtained by the top of the VB and the bottom of the CB, represented in blue color in Fig. 5b. The VB is in the M points, whereas the CB is in the Γ points. The band-gap value of the BST model was calculated as 3.76 eV, which is consistent with the experimental values found in the literature (Table 3).

As shown in Table 3, the band-gap energy of the theoretical results exhibits a small mean percentage error compared to the experimental results, evidencing that our calculations agree with the experimental data. Indeed, the largest deviation was found for the experimentally obtained BST sample at 700 °C, where a slight overestimation of 20.5% of the band-gap value was observed at the M-Γ point.

3.4.2. Density of state and Mulliken analysis

Fig. 6(a and b) show the projected DOS of BST and the presence of primary atomic orbitals of Ba, Sr, O, and Ti along with the VB and CB. Some of the atoms in this structure contribute equally due to the structural symmetry. The DOS results reveal that the upper part of the VB mainly consists of O 2p (p_x, p_y, p_z) orbitals with a minor extent of Ba, Sr, and Ti atomic orbitals. In contrast, the lower part of the CB is mainly

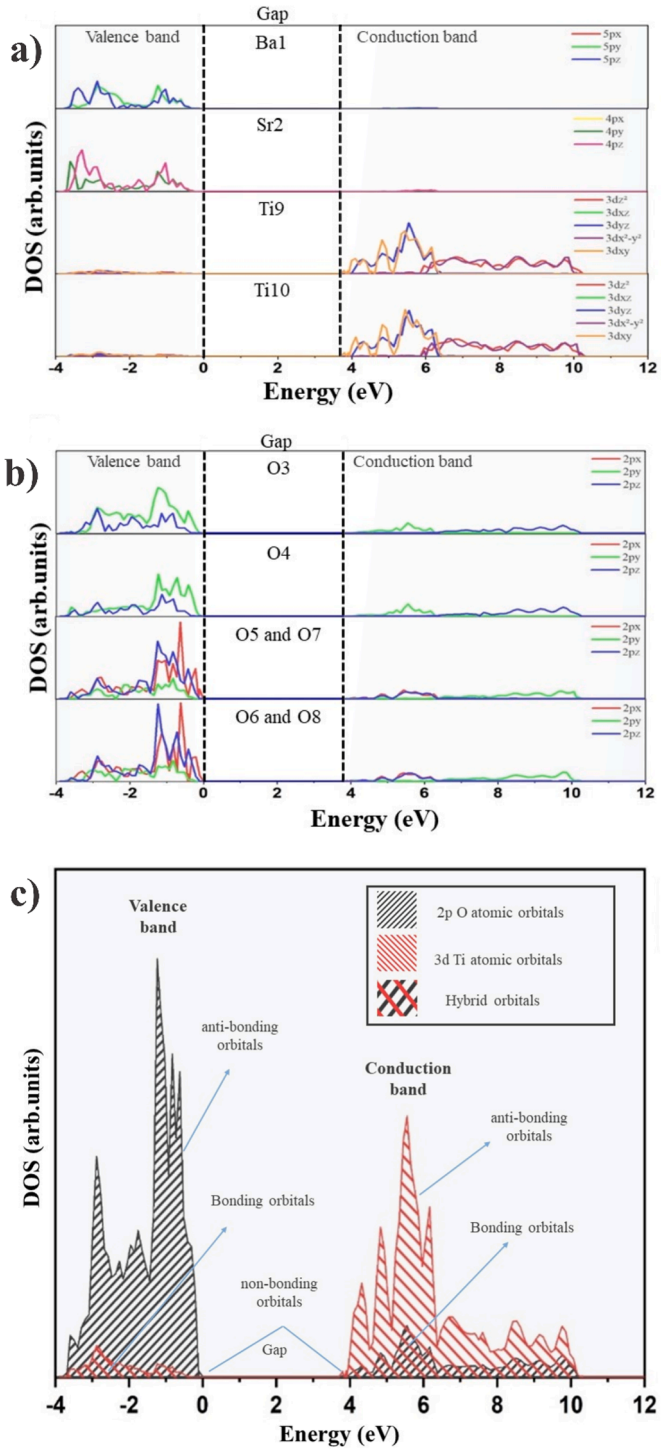

Fig. 6. Projected DOS of atoms and orbitals for BST. **(a)** Ba, Sr and Ti, **(b)** oxygen atoms, and **(c)** superposition of the titanium and oxygen atomic orbitals.

derived from Ti 3d (d_{xz}, d_{xy}, d_{yz}, d_z^2, d_{x-y}^{22}) orbitals. In Fig. 6a, the analysis of the principal components of atomic orbitals demonstrates that the Ba1 and Sr2 mainly consist of $5p_y$ and $5p_z$, and $4p_y$ and $4p_z$ atomic orbitals, respectively. No contribution of the p_x atomic orbitals can be observed. There are no equivalent contributions between the Ti9 and Ti10 atoms, being the most important contribution coming from $3d_{xy}$ and $3d_{yz}$ orbitals. Both Ti atoms in the conduction band minimum (CBM) contribute to Ti ($3d_{xy}$) states.

Fig. 6b shows the atomic orbitals for all oxygen groups, specifically

Table 4
Theoretical results for overlap population (in m|e|) of A-O and M–O bonds in the BST structures.

Overlap Populations (|e|)					
A-O		B-Oz		B-Oxy	
Ba1	Sr1	Ti9	Ti10	Ti9	Ti10
-0.008	-0.007	0.0615	0.062	0.068	0.068

$2p_x$, $2p_y$, and $2p_z$ atomic orbitals in the VB. For O3 and O4 atoms, the most significant contribution comes from $2p_y$ and $2p_z$ atomic orbitals. No contribution of the $2p_x$ orbitals can be observed. The projected DOS indicates an equivalent contribution between O5 and O7, and a different equivalence between O6 and O8. For the two equivalent oxygen groups, the most significant contribution comes from $2p_x$ and $2p_y$ atomic orbitals. The valence band maximum (VBM) is mainly composed of O $2p_y$ and $2p_x$ atomic orbitals.

The orbitals present in the VBM for all oxygen atoms summed with the Ti orbital in the CBM are responsible for the hybrid state in the BST structure.

The superposition of the projected DOS in Fig. 6c demonstrates that the hybridization occurs between titanium and oxygen atoms from approximately -4 to 0 eV and 3.76 to 10 eV for the VB and the CB, respectively, characterizing bonding orbitals in these regions. This fact suggests the covalent character of the Ti-O chemical bond. In the VB, the anti-bonding orbitals indicate that the electronic repulsion is more accentuated for the O atoms than for Ti atoms in the lattice. In contrast, these atoms exhibit inverse behavior in the CB.

The theoretical results obtained from the Mulliken population analysis [89] applied to the atomic charge (Table S2) were used to analyze the electronic density distribution in the BST structure. The choice of the Mulliken partition is arbitrary since there is no single method for partitioning the charge density. Mulliken charges show positive charges on the Ba, Sr, and Ti cations and negative charges on O anions. The values of Ti and O charges are not close to those expected for the ionic charge in the tetragonal structure (Ti^{4+} and O^{2-}). The O3 atom presents the lowest total charge value compared to the O4-O8 atoms. This behavior occurs because O3 is slightly displaced from the structure symmetry center, favoring a reduced interaction among Ba1, Ti10, O5,

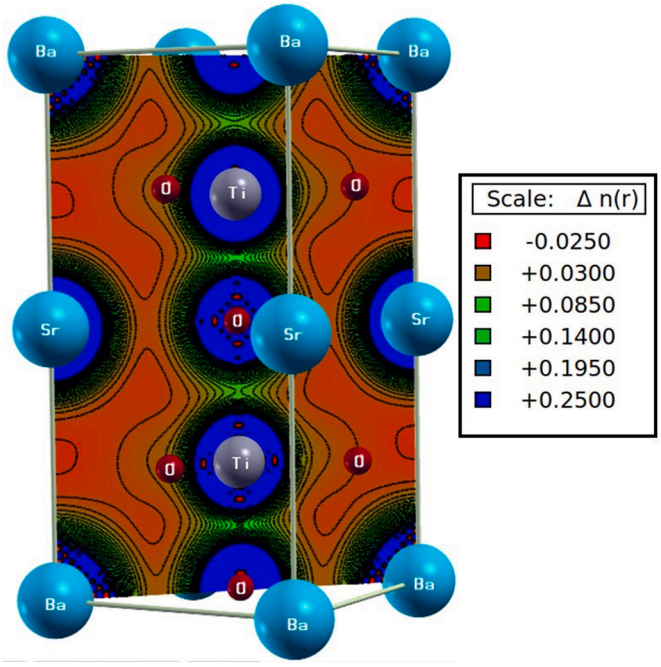

Fig. 7. Charge density maps for the BST structure.

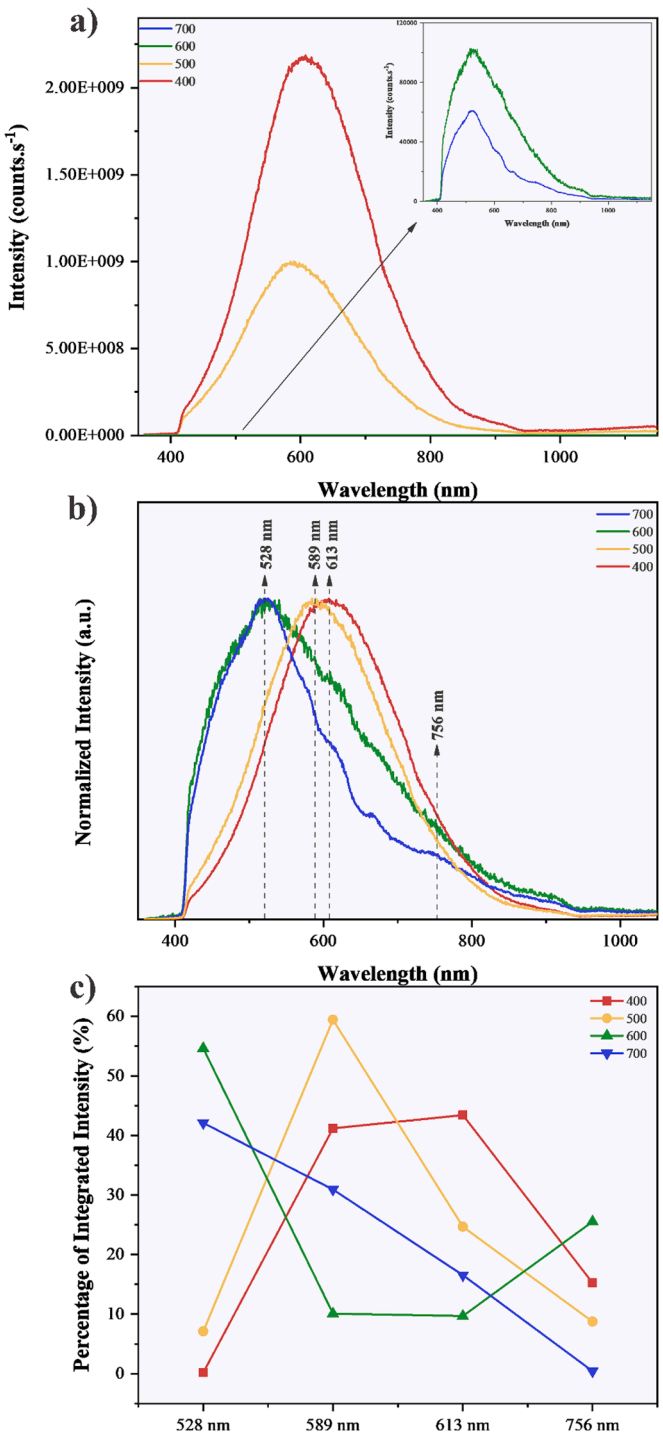

Fig. 8. **(a)** PL spectra at room temperature, **(b)** normalized intensity of PL spectra, and **(c)** deconvolution percentage of the 528, 589, 613 and 756 nm components of the PL spectra of BST samples.

and O7 atoms. As shown in Table S2, there is a different charge value between the two O groups (O5, O7 to O6, O8) located in basal plane. The difference of values can be attributed to the non-equivalent contribution of the Ti atoms in the projected DOS (Fig. 6a), generating a heterogeneous interaction field. The cation charges for Ba1 and Sr2 were found to be close to the expected values (Ba^{2+} and Sr^{2+}, respectively).

The overlap population results were obtained for A-O, B-Oz, and B-Oxy planes (Table 4). In general, the total overlap population for any pair of atoms is composed of positive (bonding) and negative (antibonding) contributions [70]. A simple way to understand the bond characteristics in ABO_3 structures is from the analysis of cation-oxygen interaction.

In this study, the negative values between Ba-O and Sr-O indicate a predominant ionic character for such chemical bonds due to an ineffective overlap between the atomic orbitals. In contrast, the positive values obtained for B-Oz and B-Oxy reveal the dominant covalent character due to the effective overlap of the atomic orbitals, characterizing an accumulation of electronic density in the internuclear region.

The difference in the B-Oz overlap for Ti9 and Ti10 is attributed to the off-centering displacement of the O3 atom caused by the structural disorder.

Finally, the bond character and charge distribution for the BST models were investigated by electronic density isolines (Fig. 7). An isoline is a set of equal value points in a data domain showing the electron density around the atomic nucleus. Colors can be used in the plane of the charge density maps to represent the charge density distribution. These results were obtained from the optimized wave function of the structures. The crystallographic plane was chosen as a vertical plane in the (110) direction containing Ba, Sr, Ti, and O atoms. The calculated charge density maps clearly display electronic paths (green color in Fig. 7) located among O3-Ti10-O4-Ti9-O3 bonds in the (110) direction. These electronic paths were then classified as bonding paths that enable an electron sharing mechanism among $[BO_6]$ octahedral clusters designed as $[TiO_6]$-$[TiO_6]$. An analysis of Fig. 7 clearly shows that the bond between A (Ba, Sr) and $[TiO_6]$ is strong ionic, while a covalent bonding nature is visible between Ti and O, resulting in the hybridization between the O (2p) and the Ti (3d) states.

3.5. Photoluminescence

PL measurements were performed to investigate the BST powders' structural order at the medium range. Besides, this technique is a sensitive tool for defects. Fig. 8 shows the PL spectra of the samples calcinated at different temperatures. For all samples, we can observe a broadband emission in the visible region, typical of multiphonon processes [90,91]. Therefore, the recombination of electron/hole pair ($e' - h^{\bullet}$) occurs by several paths due to the density of intermediate energy levels within the band-gap generated by structural order-disorder effects [92]. Fig. 8a shows an abrupt reduction in the characteristic emission of the samples from 600°C, which is attributed to the increase of the degree of order at long–and especially–short ranges, decreasing the number of defects in the forbidden region. These results are consistent with those observed by XRD and Raman and the estimated E_{gap} values.

Fig. 8b shows the normalized PL emissions of the samples. For samples calcined at 400 and 500°C, a maximum characteristic emission is centered in the orange region (613 and 589 nm, respectively), while those calcined at 600 and 700°C have a maximum emission in the green region (528 nm). This occurs because the increase in the system order as a function of temperature changes the type of defect present in the samples. In the samples at a lower temperature, there is a predominance of deep defects, far from the valence (VB) and conduction bands (CB). On the contrary, the samples at higher temperature shallow defects located close to the VB and the CB are predominant [93,94]. Thus, the defects present in the samples mostly change from deep (normally related to oxygen vacancies) to shallow (related to intrinsic structural defects) [95]. This effect is evidenced by Fig. 8c, which shows the percentage of each component of the characteristic emission for each sample (located at 528, 589, 613, and 756 nm).

Moreover, through the combination of theoretical calculations for the electronic structure of BST (Figs. 5 and 6) and PL analysis (Fig. 8) it was possible to identify the electron transfer process associated with the PL properties. In the first step, the radiation excites one electron from the VBM located in the O (2p) orbitals to an empty state of the CBM dominated by Ti (3d), confirming that order-disorder effects can tailor such property through the structural arrangement of $[TiO_6]$ clusters. Therefore, for the disordered samples, the oxygen vacancies can be

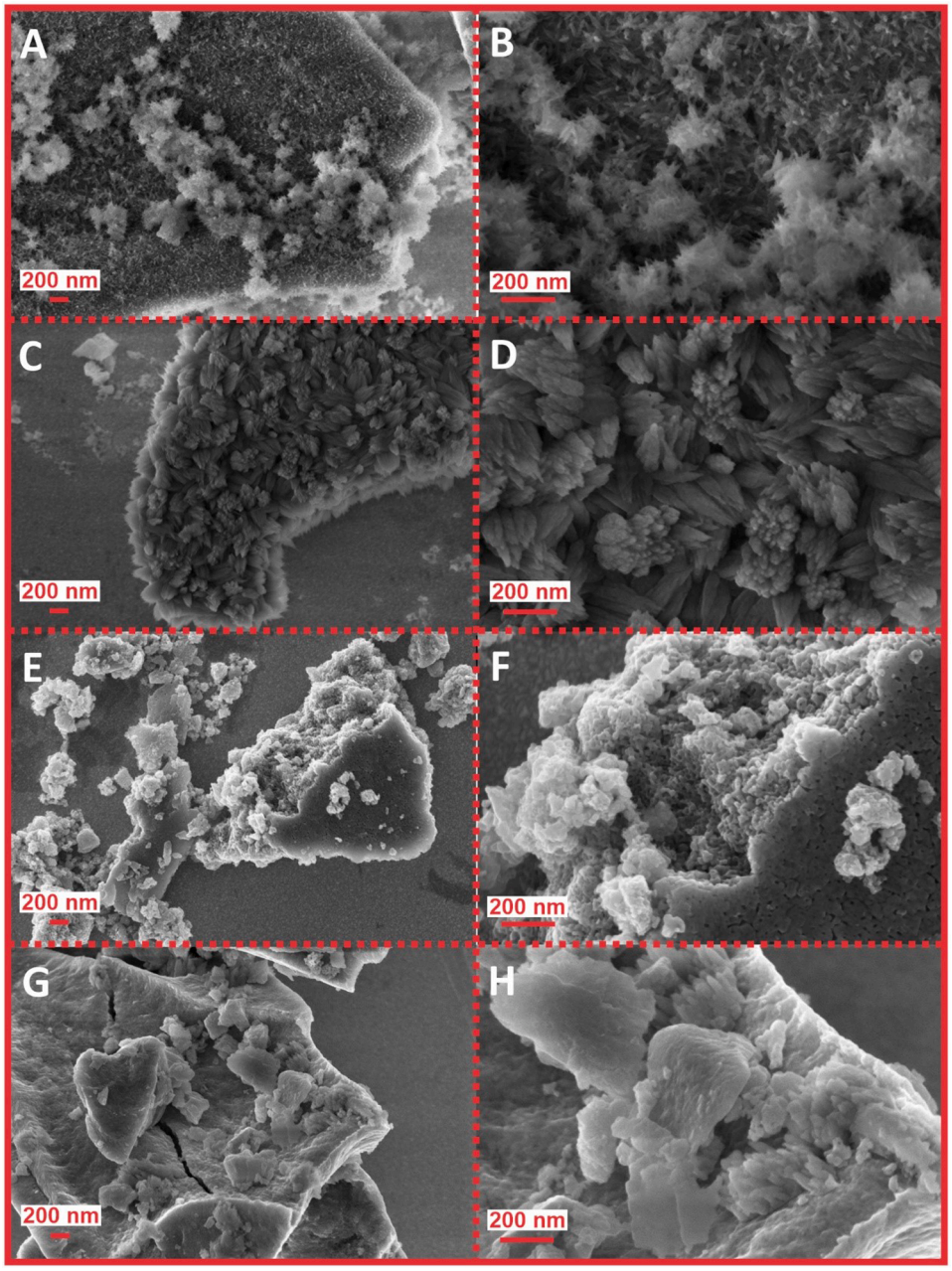

Fig. 9. FE-SEM images of BST samples calcined at **(a-b)** 400, **(c-d)** 500, **(e-f)** 600 and **(g-h)** 700 °C.

attributed to the off-centering Ti displacement in $[TiO_6]$, resulting in $[TiO_5...V_O]^x$ centers, suggesting an impurity level in the band-gap region that contributes to the PL emission. By increasing the sintering temperature, the samples can show a large degree for both short- and long-range orders, reducing the cation displacement that governs the formation of oxygen vacancies, being the common defects associated with minor disorders along the Ti-O bond lengths, which can consequently affect the position of the VBM and the CBM. Besides, the bulk/surface ratio can directly affect the PL properties, thus generating disordered centers along the exposed surfaces occupied by excited electrons or holes, as discussed in further sections.

3.6. FE-SEM analysis

FE-SEM micrographs were obtained to observe the influence of temperature on the morphology of the BST samples (Fig. 9). When the sample is calcined at 400°C (Fig. 8a and b), the formation of agglomerates constituted of nanorods is observed. As the calcination temperature increases, these nanorods are sintered for the formation of nanorices (Fig. 9c and d), followed by sample densification to form sintered solid plates (Fig. 9e–h). This phenomenon is confirmed by the loss of pores in the samples, according to Fig. 9g and h. This densification and sintering observed for the BST samples are expected since the sol-gel method is very limited in relation to size and morphology control [96]. This happens because the metallic cations are trapped in the polymeric gel formed, reducing the capacity for controlled morphological growth [97]. As a consequence, there is the appearance of plaques, which can sinter as the temperature rises.

3.7. Surface analysis

We fully optimized the low-index (001) surface to investigate the relationship between E_{surf} values and structural/electronic effects. For calculations of the BST (001) surfaces, slab models consisting of four

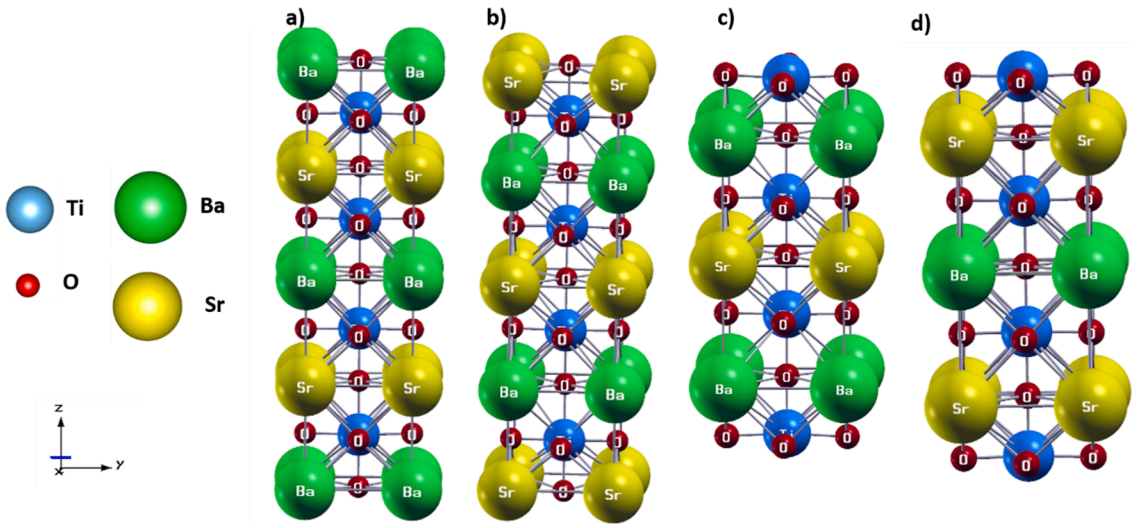

Fig. 10. Schematic 3D representation of the structures for BST (001) surfaces: **(a)** BaO-terminated surface, **(b)** SrO-terminated surface, **(c)** TiO_2-terminated surface with Ba, and **(d)** TiO_2-terminated surface with Sr.

Table 5
Calculated surface energy values (E_{surf}), band-gap, dangling bonds, area and dangling bond density (Db) for (001) surface termination of BST.

(001) Surface-Termination	E_{surf} (J/m^2)	Band-gap (eV)	Dangling bonds	Area (nm^2)	Db (nm^{-2})
BaO	1.65	3.85	4	0.1545	25.88
SrO	1.21	3.42	4	0.1545	25.88
(Sr)TiO_2	1.87	2.50	1	0.1545	6.47
(Ba)TiO_2	1.90	2.45	1	0.1545	6.47

alternating neutral AO and BO_2 layers were considered. We used symmetrical slabs and exposed equally chemical environments, i.e., the upper and lower parts of the slabs were composed of equal clusters. The slabs containing 18 and 14 layers were considered thick enough since the convergence of calculated slab total energy per BST unit was achieved. In other words, these numbers of layers were found sufficient to reach convergence. Our first and second slabs were terminated by AO planes, for example, BaO and SrO (Fig. 10a and b), and included 22 atoms. The third and fourth slabs were terminated by BO_2 planes (Fig. 10c and d) with TiO_2 planes and 18 atoms. In our calculations, both AO- and BO_2-terminated slabs were non-stoichiometric, with the following unit cell equations: $A_3A'_2Ti_4O_{13}$ and $A_2A'_1Ti_4O_{11}$.

The stability order was found to be (001- SrO) > (001- BaO) > (001- (Sr)TiO_2) > (001- (Ba)(TiO_2), as illustrated in Table 5.

In particular, by comparing the dangling bond density with the $\boldsymbol{E_{surf}}$ values for the investigated (001) surface terminations, we could observe that despite the higher D_b values for AO (A = Ba, Sr) terminations, such surfaces are more stable than A-TiO_2 surface cuts. Generally, a direct relationship between $\boldsymbol{E_{surf}}$ and $\boldsymbol{D_b}$ values is expected, i.e., for undercoordinated surfaces, it is expected an increased number of vacancies inducing greater E_{surf} values. However, for BST surfaces, the character of A-O and Ti-O chemical bonds induces a singular trend. As previously mentioned, the Ti-O chemical bonds exhibit a large covalent character in comparison to A-O (A = Ba, Sr) (Table 4). Therefore, the required energy to create a (001) surface plane exposing undercoordinated Ti centers is higher than for A metals. In this case, the covalent/ionic bond character directly affects the surface stability, being the AO (A = Ba, Sr) surface plane the most stable one, even in the presence of higher dangling bond density.

Concerning the electronic structure for the investigated (001) surface terminations, it was observed that AO (A = Ba, Sr) terminations exhibit band-gap values close to the bulk (3.76 eV – Table 3), whereas the A-TiO_2 terminations show a reduced band-gap value. This fact can be explained by the significant contributions of Ti-O bond interactions in the electronic structure for the BST bulk (Fig. 7). Indeed, as previously discussed, the VB and the CB of BST are directly associated with the hybridization of O(2p) and Ti(3d) atomic states that govern the covalent Ti-O bond path. In contrast, the more ionic A-O bond interactions exhibit a relatively small contribution for both VB and CB. In this case, the (001) surface exposure exhibiting undercoordinated Ti centers induces the creation of intermediary energy levels in the band-gap region, inducing a narrowing of the required energy for the electronic excitation, as confirmed by Fig. 11.

Now we will briefly discuss the role of BST surfaces to understand the PL properties of the as-synthesized samples. In this study, it was confirmed that AO surface terminations maintain the general pattern for the electronic structure of the BST bulk, generating few disorders along with the positions of VBM and CBM levels according to the regular distribution along the $[TiO_6]$ centers located in the inner shells of the exposed slabs, which are responsible for the control of the BST electronic structure. On the other hand, for A-TiO_2, the exposed surfaces contribute to the generation of oxygen vacancies through the exposure of undercoordinated $[TiO_5]$ centers, inducing a band-gap reduction with the creation of intermediary energy levels in comparison to the electronic structure of the BST bulk (Figs. 5 and 6). In this case, the existence of larger structural disorder effects in the sintered samples at lower temperatures can also be associated with the increased contribution of A-TiO_2 (001) surfaces, while the more ordered phase observed in the samples at higher temperatures can be attributed to the presence of AO (001) surfaces in the BST material.

Indeed, such a hypothesis can be supported by the morphological evolution observed during the FE-SEM analysis (Fig. 9), where a clear morphological modulation can be associated with the increase of the sintering temperature. In this case, the samples obtained at lower temperatures can exhibit a well-defined arrangement related to the presence of A-TiO_2 (001) surfaces, while the other samples can exhibit a large contribution of AO (001) surfaces or other surface planes such as (101). Therefore, when combining all employed analyses, the role of Ti-O chemical bonds in the control of the structural, electronic, and optical properties of the BST material is highlighted and explained in details, contributing to an in-depth understanding of the major keys that control the optical properties of mixed perovskite materials.

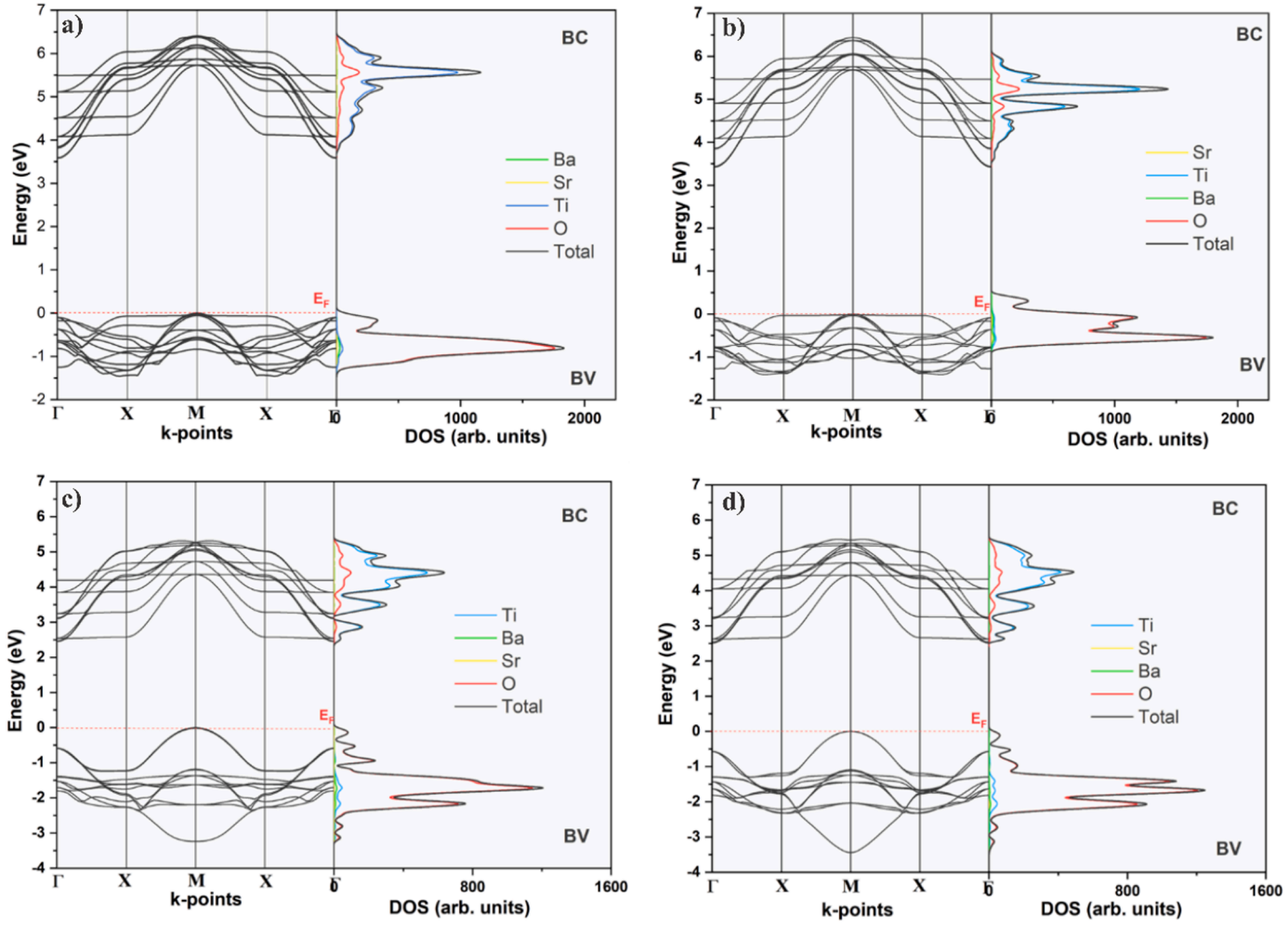

Fig. 11. Band structure and total-resolved density of states (DOS) profiles for BST (001) surfaces: (a) BaO-terminated surface, (b) SrO-terminated surface, (c) TiO_2-terminated surface with Ba, and (d) TiO_2-terminated surface with Sr.

4. Conclusion

In this study, DFT calculations and experimental techniques were combined to investigate the structural, electronic, and photoluminescent properties of as-synthesized BST samples obtained by the polymeric precursor method. The crystalline structure of the obtained samples as a function of sintering temperature was determined by XRD analysis, revealing a tetragonal symmetry with short- and long-range structural disorders classified with the aid of Raman spectroscopy, UV-Vis analysis, and PL properties. In particular, DFT calculations confirmed the existence of such structural disorder along with the BST crystalline structure, which induces two distinct bonding environments for both [AO_{12}] (A = Ba, Sr) and [TiO_6] clusters, respectively, being the first one dominated by ionic features, while the second one exhibits a large covalent component. UV–Vis spectroscopy and PL measurements were used to investigate the BST optical properties. These results, combined with experimental band-gap analysis, helped us identify the dominant role of bonding Ti-O paths in BST electronic structures. Moreover, DFT calculations were also applied to the (001) surfaces of BST, indicating that the A-O and Ti-O bond characters affect the surface stabilization and the electronic structure of the exposed surfaces, thus confirming that (001) surfaces with undercoordinated Ti centers exhibit a narrowed band-gap in comparison to the bulk, which makes this type of material a suitable choice for optical and electronic applications. Therefore, the combined experimental and theoretical approach successfully explained the BST properties at the atomic-level viewpoint, enabling understanding of the major question involving such perovskite material.

CRediT authorship contribution statement

Weber Duarte Mesquita: Conceptualization, Formal analysis, Investigation, Writing – original draft, Writing – review & editing, Visualization. **Marisa Carvalho de Oliveira:** Conceptualization, Formal analysis, Investigation, Writing – original draft, Writing – review & editing, Visualization. **Marcelo Assis:** Conceptualization, Formal analysis, Investigation, Writing – original draft, Writing – review & editing, Visualization. **Renan Augusto Pontes Ribeiro:** Conceptualization, Formal analysis, Investigation, Writing – original draft, Writing – review & editing, Visualization. **Ariadne Canedo Eduardo:** Conceptualization, Formal analysis, Investigation, Writing – original draft, Writing – review & editing, Visualization. **Marcio Daldin Teodoro:** Conceptualization, Formal analysis, Investigation, Writing – original draft, Writing – review & editing, Visualization. **Gilmar Eugenio Marques:** Conceptualization, Formal analysis, Investigation, Writing – original draft, Writing – review & editing, Visualization. **Mário Godinho Júnior:** Writing – review & editing, Visualization, Project administration, Funding acquisition. **Elson Longo:** Writing – review & editing, Visualization, Project administration, Funding acquisition. **Maria Fernanda do Carmo Gurgel:** Writing – review & editing, Visualization, Supervision, Project administration.

Declaration of Competing Interest

The author(s) declare(s) that there is no conflict of interest regarding the publication of this article.

Acknowledgment

The authors would like to thank the following Brazilian research financing institutions for the financial support: the National Council for Scientific and Technological Development – *CNPQ*, the Coordination for the Improvement of Higher Education Personnel – *CAPES*, the Goiás Research Foundation – FAPEG, the São Paulo Research Foundation – FAPESP (2013/07296-2), the Federal University of Catalão and the Federal University of São Carlos. M. C. Oliveira acknowledges the financial support from FAPESP (2021/01651-1). The authors also thank the National Laboratory for Scientific Computing (*LNCC*) and the High-Performance Computing Center (NACAD) at the Federal University of Rio de Janeiro (COPPE-UFRJ) for providing the computational resources of Lobo Carneiro supercomputer.

Supplementary materials

Supplementary material associated with this article can be found, in the online version, at doi:10.1016/j.materresbull.2021.111442.

References

[1] T. Zhang, et al., High energy storage density at low electric field of ABO_3 antiferroelectric films with ionic pair doping, Energy Storage Mater. 18 (2019) 238–245.
[2] Z. Xu, et al., Effects of sintering temperature on the properties of donor-acceptor codoped $Ba_{0.67}Sr_{0.33}TiO_3$ ceramics for pyroelectric infrared detector applications, Ceram. Int. 40 (3) (2014) 4617–4621.
[3] C.V.G. Reddy, et al., Noble metal additive modulation of gas sensitivity of $BaSnO_3$, explained by a work function based model, Thin Solid Films 348 (1) (1999) 261–265.
[4] K.-T. Kim, et al., Microwave characteristics of sol-gel based Ag-doped $(Ba_{0.6}Sr_{0.4})TiO_3$ thin films, Thin Solid Films 565 (2014) 172–178.
[5] A.R. Albuquerque, et al., DFT study with inclusion of the grimme potential on anatase TiO_2: structure, electronic, and vibrational analyses, J. Phys. Chem. A 116 (47) (2012) 11731–11735.
[6] A.R. Jurelo, et al., Structural, vibrational and electronic properties of the superconductor Cu_xTiSe_2: theoretical and experimental insights, PCCP 20 (42) (2018) 27011–27018.
[7] Q. Ji, et al., The role of oxygen vacancies of ABO_3 perovskite oxides in the oxygen reduction reaction, Energy Environ. Sci. 13 (5) (2020) 1408–1428.
[8] D. Wrana, et al., In situ study of redox processes on the surface of $SrTiO_3$ single crystals, Appl. Surf. Sci. 432 (2018) 46–52.
[9] R. Eglitis, S.P. Kruchinin, Ab initio calculations of ABO_3 perovskite (001), (011) and (111) nano-surfaces, interfaces and defects, Mod. Phys. Lett. B 34 (19n20) (2020), 2040057.
[10] C. Rodenbücher, et al., Stability and decomposition of perovskite-type titanates upon high-temperature reduction, Phys. Status Solidi RRL 11 (9) (2017), 1700222.
[11] R.I. Eglitis, Ab initio calculations of $CaZrO_3$, $BaZrO_3$, $PbTiO_3$ and $SrTiO_3$ (001), (011) and (111) surfaces as well as their (001) interfaces, Integr. Ferroelectr. 196 (1) (2019) 7–15.
[12] R.I. Eglitis, Theoretical modelling of the energy surface (001) and topology of $CaZrO_3$ perovskite, Ferroelectrics 483 (1) (2015) 75–85.
[13] G.-Z. Zhu, G. Radtke, G.A. Botton, Bonding and structure of a reconstructed (001) surface of $SrTiO_3$ from TEM, Nature 490 (7420) (2012) 384–387.
[14] A. Biswas, et al., Universal Ti-rich termination of atomically flat $SrTiO_3$ (001), (110), and (111) surfaces, Appl. Phys. Lett. 98 (5) (2011), 051904.
[15] M.S.J. Marshall, et al., Atomic and electronic surface structures of dopants in oxides: STM and XPS of Nb- and La-doped $SrTiO_3$ (001), Phys. Rev. B 83 (3) (2011), 035410.
[16] T. Shimizu, et al., Scanning tunneling microscopy and spectroscopy observation of reduced $BaTiO_3$(100) surface, Jpn. J. Appl. Phys. 34 (Part 2, No. 10A) (1995) L1305–L1308.
[17] R. Courths, Ultraviolet photoelectron spectroscopy (UPS) and LEED studies of $BaTiO_3$ (001) and $SrTiO_3$ (100) surfaces, Phys. Status Solidi B 100 (1) (1980) 135–148.
[18] R. Shimizu, et al., Effect of oxygen deficiency on $SrTiO_3$(001) surface reconstructions, Appl. Phys. Lett. 100 (26) (2012), 263106.
[19] T. Kubo, H. Orita, H. Nozoye, Atomic structures of the defective $SrTiO_3$ (001) surface, Phys. Chem. Chem. Phys. 13 (37) (2011) 16516–16519.
[20] R.I. Eglitis, et al., Comparative ab initio calculations of ReO_3, $SrZrO_3$, $BaZrO_3$, $PbZrO_3$ and $CaZrO_3$ (001) surfaces, Crystals 10 (9) (2020) 745.
[21] S. Piskunov, R.I. Eglitis, Comparative ab initio calculations of $SrTiO_3/BaTiO_3$ and $SrZrO_3/PbZrO_3$ (001) heterostructures, Nucl. Instrum. Methods Phys. Res. Sect. B 374 (2016) 20–23.
[22] R.I. Eglitis, S. Piskunov, Y.F. Zhukovskii, Ab initio calculations of $PbTiO_3/SrTiO_3$ (001) heterostructures, Phys. Status Solidi C 13 (10-12) (2016) 913–920.
[23] M. Sokolov, et al., Ab initio hybrid DFT calculations of $BaTiO_3$ bulk and BaO-terminated (001) surface F-centers, Int. J. Mod. Phys. B 31 (31) (2017), 1750251.
[24] R.I. Eglitis, A.I. Popov, Ab initio calculations for the polar (0 0 1) surfaces of $YAlO_3$, Nucl. Instrum. Methods Phys. Res. Sect. B 434 (2018) 1–5.
[25] R.I. Eglitis, A.I. Popov, Systematic trends in (001) surface ab initio calculations of ABO_3 perovskites, J. Saudi Chem. Soc. 22 (4) (2018) 459–468.
[26] R.I. Eglitis, First-principles calculations of $SrZrO_3$ (001) surfaces, Integr. Ferroelectr. 123 (1) (2011) 26–31.
[27] C. Li, K.C.K. Soh, P. Wu, Formability of ABO_3 perovskites, J Alloy Compd 372 (1) (2004) 40–48.
[28] C. Li, et al., Formability of ABX_3 (X = F, Cl, Br, I) halide perovskites, Acta Cryst. B 64 (6) (2008) 702–707.
[29] S. Chauhan, et al., Sol-gel synthesis, crystalline phase, optical absorption, and photo-luminescence behavior of cerium-doped $(Ba_{0.5}Sr_{0.5})FeO_{3-\delta}$ powders, Mater. Res. Express 6 (10) (2019), 105520.
[30] H. Zhu, P. Zhang, S. Dai, Recent advances of lanthanum-based perovskite oxides for catalysis, ACS Catal. 5 (11) (2015) 6370–6385.
[31] B. Scherrer, et al., Correlation between electrical properties and thermodynamic stability of $ACoO_{3-\delta}$ perovskites (A = La, Pr, Nd, Sm, Gd), Phys. Rev. B 84 (8) (2011), 085113.
[32] D.S.L. Pontes, et al., Influence of a co-substituted A-site on structural characteristics and ferroelectricity of $(Pb,Ba,Ca)TiO_3$ complex perovskites: analysis of local-, medium- and long-range order, J. Sol-Gel Sci. Technol. 69 (3) (2014) 605–616.
[33] L.P. Curecheriu, L. Mitoseriu, A. Ianculescu, Nonlinear dielectric properties of $Ba_{1-x}Sr_xTiO_3$ ceramics, J. Alloys Compd. 482 (1) (2009) 1–4.
[34] A. Ioachim, et al., Barium strontium titanate-based perovskite materials for microwave applications, Prog. Solid State Chem. 35 (2) (2007) 513–520.
[35] A.E. Souza, et al., Photoluminescence of $SrTiO_3$: influence of particle size and morphology, Cryst. Growth Des. 12 (11) (2012) 5671–5679.
[36] M. Vijatović, J. Bobić, B. Stojanović, History and challenges of barium titanate: part I, Sci. Sinter. 40 (2) (2008) 155–165.
[37] M.C. Oliveira, et al., Temperature dependence on phase evolution in the $BaTiO_3$ polytypes studied using ab initio calculations, Int. J. Quantum Chem. 120 (1) (2020) e26054.
[38] L. Zhou, P.M. Vilarinho, J.L. Baptista, Dependence of the structural and dielectric properties of $Ba_{1-x}Sr_xTiO_3$ ceramic solid solutions on raw material processing, J. Eur. Ceram. Soc. 19 (11) (1999) 2015–2020.
[39] P. Scherrer, Bestimmung der Grosse und der inneren Struktur von Kolloidteilchen mittels Rontgenstrahlen, Göttinger Nachrichten Gesell 2 (1918) 98–100.
[40] A. Weibel, et al., The big problem of small particles: a comparison of methods for determination of particle size in nanocrystalline anatase powders, Chem. Mater. 17 (9) (2005) 2378–2385.
[41] A. Guinier, X-Ray Diffraction in Crystals, Imperfect Crystals, and Amorphous Bodies, Dover Publications, 1994.
[42] G.K. Williamson, W.H. Hall, X-ray line broadening from filed aluminium and wolfram, Acta Metall. 1 (1) (1953) 22–31.
[43] R. Dovesi, et al., CRYSTAL14: a program for the ab initio investigation of crystalline solids, Int. J. Quantum Chem. 114 (19) (2014) 1287–1317.
[44] C. Lee, W. Yang, R.G. Parr, Development of the Colle-Salvetti correlation-energy formula into a functional of the electron density, Phys. Rev. B 37 (2) (1988) 785–789.
[45] A.D. Becke, Correlation energy of an inhomogeneous electron gas: a coordinate-space model, J. Chem. Phys. 88 (2) (1988) 1053–1062.
[46] J. Maul, et al., Thermal properties of the orthorhombic $CaSnO_3$ perovskite under pressure from ab initio quasi-harmonic calculations, Theor. Chem. Acc. 135 (2) (2016) 36.
[47] M.C. Oliveira, et al., Mechanism of photoluminescence in intrinsically disordered $CaZrO_3$ crystals: first principles modeling of the excited electronic states, J. Alloys Compd. 722 (2017) 981–995.
[48] V.M. Longo, et al., First principles calculations on the origin of violet-blue and green light photoluminescence emission in $SrZrO_3$ and $SrTiO_3$ perovskites, Theor. Chem. Acc. 124 (5) (2009) 385.
[49] https://www.crystal.unito.it/basis-sets.php. https://www.crystal.unito.it/basis-sets.php. 2020 [cited 2020 07/08/2020]; Available from: https://www.crystal.unito.it/basis-sets.php.
[50] K. Momma, F. Izumi, VESTA 3 for three-dimensional visualization of crystal, volumetric and morphology data, J. Appl. Crystallogr. 44 (6) (2011) 1272–1276.
[51] H.J. Monkhorst, J.D. Pack, Special points for Brillouin-zone integrations, Phys. Rev. B 13 (12) (1976) 5188–5192.
[52] C. Paiva-Santos, et al., Influência da adiçao de La e Sr nos parâmetros estruturais do $PbTiO_3$, Cerâmica 35 (1989) 153.
[53] J.R. Sambrano, et al., Theoretical analysis of the structural deformation in Mn-doped $BaTiO_3$, Chem. Phys. Lett. 402 (4) (2005) 491–496.
[54] J. Foresman, E. Frish, Exploring Chemistry, Gaussian Inc., Pittsburg, USA, 1996.
[55] K. Manjunatha, et al., Structural, electronic, vibrational and magnetic properties of Zn^{2+} substituted $MnCr_2O_4$ nanoparticles, J. Magn. Magn. Mater. 502 (2020), 166595.
[56] J. Andrés, et al., Effects of surface stability on the morphological transformation of metals and metal oxides as investigated by first-principles calculations, Nanotechnology 26 (40) (2015), 405703.

[57] T. Wei, et al., Novel optical temperature sensor based on emission in Pr^{3+} doped ferroelectric $Ba_{0.7}Sr_{0.3}TiO_3$, RSC Adv. 8 (42) (2018) 23996–24001.
[58] C.M. Holl, et al., Compression of witherite to 8 GPa and the crystal structure of $BaCO_3$II, Phys. Chem. Miner. 27 (7) (2000) 467–473.
[59] M.C.F. Alves, et al., Influence of the modifier on the short and long range disorder of stannate perovskites, J. Alloys Compd. 476 (1) (2009) 507–512.
[60] M.A.F. de Souza, et al., Synthesis and characterization of Sr1−xMgxTiO3 obtained by the polymeric precursor method, Mater. Lett. 59 (5) (2005) 549–553.
[61] M.A.F. Souza, et al., Thermal and structural characterization OF $Sr_{1-x}Co_xTiO_3$ obtained by polymeric precursor method, J. Therm. Anal. Calorim. 79 (2) (2005) 407–410.
[62] D.S. Melo, et al., Lanthanum-based perovskites obtained by the polymeric precursor method, J. Mater. Sci. 43 (2) (2008) 551–556.
[63] M.R. Cassia-Santos, et al., Thermal and structural investigation of $(Sn_{1-x}Ti_x)O_2$ obtained by the polymeric precursor method, J. Therm. Anal. Calorim. 79 (2) (2005) 415–420.
[64] S.A. Eliziário, et al., Black and green pigments based on chromium–cobalt spinels, Mater. Chem. Phys. 129 (1) (2011) 619–624.
[65] T.R. Giraldi, et al., Effect of synthesis parameters on the structural characteristics and photocatalytic activity of ZnO, Mater. Chem. Phys. 136 (2) (2012) 505–511.
[66] A.C. Chaves, et al., Photoluminescence in disordered Zn_2TiO_4, J. Solid State Chem. 179 (4) (2006) 985–992.
[67] B. Vigneshwaran, et al., Study of low temperature-dependent structural, dielectric, and ferroelectric properties of $Ba_xSr_{(1-x)}TiO_3$ (x= 0.5, 0.6, 0.7) ceramics, J. Mater. Sci. - Mater. Electron. 31 (2020) 10446–10459.
[68] O.P. Thakur, C. Prakash, D.K. Agrawal, Microwave synthesis and sintering of $Ba_{0.95}Sr_{0.05}TiO_3$, Mater. Lett. 56 (6) (2002) 970–973.
[69] J. Ćirković, et al., Dielectric and ferroelectric properties of BST ceramics obtained by a hydrothermally assisted complex polymerization method, Ceram. Int. 41 (9, Part A) (2015) 11306–11313.
[70] S.W. Kim, et al., Electrical properties and phase of $BaTiO_3$–$SrTiO_3$ solid solution, Ceram. Int. 39 (2013) S487–S490.
[71] Y. Zhang, et al., Abnormal cubic-tetragonal phase transition of barium strontium titanate nanoparticles studied by in situ Raman spectroscopy and transmission electron microscopy heating experiments, Appl. Phys. Lett. 107 (18) (2015), 182902.
[72] R. Shannon, Revised effective ionic radii and systematic studies of interatomic distances in halides and chalcogenides, Acta Crystallogr. A 32 (5) (1976) 751–767.
[73] M. Sukumar, et al., Facile microwave assisted combustion synthesis, structural, optical and magnetic properties of $La_{2-x}Sr_xCuO_4$ ($0 \leq x \leq 0.5$) perovskite nanostructures, J. Magn. Magn. Mater. 465 (2018) 48–57.
[74] J. Dutra, et al., Optical and structural characterization of lanthanum orthoferrites doped with chromium and aluminum, Cerâmica 64 (371) (2018) 413–417.
[75] U.D. Venkateswaran, V.M. Naik, R. Naik, High-pressure Raman studies of polycrystalline $BaTiO_3$, Phys. Rev. B 58 (21) (1998) 14256–14260.
[76] S.Y. Wang, et al., Raman spectroscopy studies of Ce-doping effects on $Ba_{0.5}Sr_{0.5}TiO_3$ thin films, J. Appl. Phys. 99 (1) (2006), 013504.
[77] I.A. Souza, et al., Theoretical and experimental study of disordered $Ba_{0.45}Sr_{0.55}TiO_3$ photoluminescence at room temperature, Chem. Phys. 322 (3) (2006) 343–348.
[78] V.S. Puli, et al., Synthesis and characterization of lead-free ternary component BST–BCT–BZT ceramic capacitors, J. Adv. Dielectr. 04 (02) (2014), 1450014.
[79] L.Z. Cao, et al., Influence of stress on Raman spectra in $Ba_{1-x}Sr_xTiO_3$ thin films, J. Phys. D 39 (13) (2006) 2819–2823.
[80] D.A. Tenne, et al., Lattice dynamics in $Ba_xSr_{1-x}TiO_3$ single crystals: a Raman study, Phys. Rev. B 70 (17) (2004), 174302.
[81] R. Ganjir, P.K. Bajpai, Influence of Co doping on the structural, dielectric and raman properties of $Ba_{0.75}Sr_{0.25}Ti_{1-x}Co_xO_3$, J. Electron. Mater. 48 (1) (2019) 634.
[82] P. Durán, et al., $BaTiO_3$ formation by thermal decomposition of a (BaTi)-citrate polyester resin in air, J. Mater. Res. 16 (1) (2011) 197–209.
[83] R.S. Katiyar, M. Jain, Y.I. Yuzyuk, Raman spectroscopy of bulk and thin-layer (Ba, Sr)TiO_3 ferroelectrics, Ferroelectrics 303 (1) (2004) 101–105.
[84] D.L. Wood, J. Tauc, Weak absorption tails in amorphous semiconductors, Phys. Rev. B 5 (8) (1972) 3144–3151.
[85] F. Urbach, The long-wavelength edge of photographic sensitivity and of the electronic absorption of solids, Phys. Rev. 92 (5) (1953) 1324.
[86] F.M. Pontes, et al., Ferroelectric and optical properties of $Ba_{0.8}Sr_{0.2}TiO_3$ thin film, Jpn. J. Appl. Phys. 91 (9) (2002) 5972–5978.
[87] K.-H. Cho, et al., Microstructure and properties of highly elongated $(Ba_{0.5}Sr_{0.5})TiO_3$ thin films by applied electric field annealing, Curr. Appl. Phys. 11 (3, Supplement) (2011) S106–S109.
[88] T. Bayrak, C. Ozgit-Akgun, E. Goldenberg, Structural, optical and electrical characteristics $BaSrTiO_x$ thin films: effect of deposition pressure and annealing, J. Non-Cryst. Solids 475 (2017) 76–84.
[89] R.S. Mulliken, Electronic population analysis on LCAO–MO molecular wave functions. I, J. Chem. Phys. 23 (10) (1955) 1833–1840.
[90] P.F.S. Pereira, et al., ZnWO4 nanocrystals: synthesis, morphology, photoluminescence and photocatalytic properties, Phys. Chem. Chem. Phys. 20 (3) (2018) 1923–1937.
[91] J. Milanez, et al., The role of oxygen vacancy in the photoluminescence property at room temperature of the $CaTiO_3$, J Appl Phys 106 (4) (2009), 043526.
[92] Z. Amouzegar, et al., Microwave engineering of ZnWO4 nanostructures: towards morphologically favorable structures for photocatalytic activity, Ceram. Int. 41 (7) (2015) 8352–8359.
[93] A.C.M. Tello, et al., Microwave-driven hexagonal-to-monoclinic transition in $BiPO_4$: an in-depth experimental investigation and first-principles study, Inorg. Chem. 59 (11) (2020) 7453–7468.
[94] J.S. de, M.J.S. Chaves, et al., Environmental remediation properties of Bi_2WO_6 hierarchical nanostructure: a joint experimental and theoretical investigation, J. Solid State Chem. 274 (2019) 270–279.
[95] E. Orhan, et al., Theoretical and experimental study of the relation between photoluminescence and structural disorder in barium and strontium titanate thin films, J. Eur. Ceram. Soc. 25 (12) (2005) 2337–2340.
[96] V. Somani, S.J. Kalita, Synthesis and characterization of nanocrystalline barium strontium titanate powder via sol-gel processing, J. Electroceram. 18 (1) (2007) 57–65.
[97] L. Dimesso, Pechini processes: an alternate approach of the sol-gel method, preparation, properties, and applications, in: L. Klein, M. Aparicio, A. Jitianu (Eds.), Handbook of Sol-Gel Science and Technology: Processing, Characterization and Applications, Springer International Publishing, Cham, 2018, pp. 1067–1088.